Research Square

Preprints are preliminary reports that have not undergone peer review.
They should not be considered conclusive, used to inform clinical practice,
or referenced by the media as validated information.

Controlling the optical properties and analyzing mechanical, dielectric characteristics of MgO doped (PVA–PVP) blend by altering the doping content for multifunctional microelectronic devices

M.I. Mohammed (mrftismail@yahoo.com)
Ain Shams University Faculty of Education https://orcid.org/0000-0001-9402-8140

Research Article

Keywords: MgO/ (PVP-PVA) nanocomposites, XRD/ SEM analysis, Optical band gap, Mechanical properties, Dielectric properties, nonlinear I-V curve

Posted Date: March 21st, 2022

DOI: https://doi.org/10.21203/rs.3.rs-1450356/v1

License: This work is licensed under a Creative Commons Attribution 4.0 International License.
Read Full License

Controlling the optical properties and analyzing mechanical, dielectric characteristics of MgO doped (PVA–PVP) blend by altering the doping content for multifunctional microelectronic devices.

M.I. Mohammed

Nanoscience Laboratory for Environmental and Biomedical Applications (NLEBA), Metallurgical Lab.1., Department of Physics, Faculty of Education, Ain Shams University, Roxy, 11757 Cairo, Egypt.

Abstract

The solution-cast method was used to synthesize magnesia (MgO) nanoparticles filled poly(vinyl alcohol) (PVA) and poly(vinyl pyrrolidone) (PVP) blend matrix (80/20 wt %) based polymeric nanocomposite (PNC) films (i.e., [PVA–PVP]–x wt % MgO; x=0, 0.06, 0.3, 0.6, 3.1, and 6.25). Most of these PNC materials structures are amorphous, according to an X-ray diffraction investigation. The blend surface was smooth and homogeneous under SEM, confirming PVA and PVP compatibility. MgO loading, on the other hand, enhanced the surface roughness. According to optical investigations, the films transmittance, Urbach's energy, and energy bandgap decreased as the Mg^{+2} -ions increased. Tensile strength has also improved from 5.92 MPa to 10.65 MPa, while Young's modulus has enhanced from 51.16 to 166.4 MPa. From 100 Hz to 1 MHz, the dielectric and electrical spectra of these films were measured. Due to the nanoconfinement effect, it has been determined that the dispersion of MgO nanoparticles in the PVA–PVP blend matrix dramatically increases the dielectric permittivity. With increasing frequency, the dielectric permittivity of these PNC films decreases while the ac electrical conductivity increases. When the temperature of a PNC film is raised, a nonlinear rise in dielectric permittivity is seen, and the dc electrical conductivity of the film follows the Arrhenius law. The nonlinear I-V curves improve with increased Mg^{+2} ion concentration. The developed and engineered unique high-performance flexible nanocomposites in the field of advanced functional materials for usage in next-generation optoelectronic, gas sensors, and microelectronic devices were ascribed to the studied properties of the PNC films.

Keywords**:** MgO/ (PVP-PVA) nanocomposites; XRD/ SEM analysis; Optical band gap; Mechanical properties; Dielectric properties; nonlinear I-V curve.

Corresponding author:** ***M.I. Mohammed

Email Address: mrftismail@yahoo.com

Introduction

Hybrid polymer nanocomposites are a unique form of material with specific physical and chemical characteristics. Due to their tangible potential for a wide range of applications in environmental solutions and treating numerous environmental challenges, these nanocomposites have lately piqued researchers' interest. The complicated interaction between nanoparticles and polymer metrics is the most challenging feature of PNCs [1,2]. Large specific surfaces are produced as a result of the small dimensions, emphasizing the relevance of the polymer-nanoparticle interactions [3]. To accomplish mechanical, thermal, dielectric, optical, and electrical characteristics, it is essential to investigate the interpolation process between nanoparticles and polymer bases [4,5].

Because of its high melting point, low erosion rate, non-toxicity, and outstanding biocompatibility, nano-sized MgO has recently attracted a lot of interest [6–9]. Furthermore, its optical band gap is 4.5 eV, compared to 7.8 eV for bulk MgO's regular structure [8-10], which improves its UV blocking ability and photocatalytic activity [7]. Because of its large surface area, nano sized MgO is more efficient in wastewater treatment [10]. Ceramics, aircraft, foundry, optoelectronic materials, transparent fillers, antimicrobial agents, fire retardants, and electrochemical biosensors all use it as a protective layer [11,12].

MgO nanostructures with various morphologies have been produced using a variety of techniques. Heat treating a magnesium carbonate/poly (methyl methacrylate) composite [7] and flame spray pyrolysis [13] were used to synthesize MgO NPs with a size of 42 nm. A sol-gel method was also used to produce MgO thin films with a honeycomb-like structure [9]. Because of their unique features and possible technological uses, one-dimensional nanostructures have gotten a lot of interest. MgO nano-belts were made using a DC arc plasma jet chemical vapor deposition approach [14], while MgO nanofibers were made using a hydrothermal method [15].

Biodegradable, biocompatible, non-toxic, and easy-to-process synthetic polymers, such as poly(vinyl alcohol) (PVA) and poly(vinyl pyrrolidone) (PVP), have a wide range of biomedical, engineering, and technical uses [16,17]. When using the solution casting process, these polymers are water-soluble and produce very optically clear films. PVA film offers outstanding features such as great flexibility, elasticity, and chemical resistance, but PVP film is sometimes too weak to withstand technical treatment such as bending or stretching. These polymers films have a low permittivity and good electrical insulation; thus, they're widely

employed as a flexible dielectric material in the production of organic thin-film transistors and optoelectronic devices [18,19]. Because the hydroxyl (–OH) and carbonyl (C=O) functional polar groups present in the chain backbone of PVA and PVP, respectively, from strong interactions with a variety of inorganic nanofillers, these hydrophilic polymers are commonly used as binders and capping agents in the preparation of advanced composite materials [20-22]. The design and characterization of PVA and PVP blends have received a lot of attention over the last two decades in order to improve the potential uses of these materials in biomedical, electronics, and electrical engineering [23]. Polymer blending is a cost-effective and efficient green chemistry method for creating innovative polymeric materials with the qualities of pure polymers; however, the processing processes employed to make the blend can dramatically affect the final product's physicochemical properties. Mixing distinct characteristics of polymers to make a unique polymer blend material is often only viable if the blended polymers are highly miscible. Many spectroscopic, thermophysical, structural, and morphological research on the PVA–PVP blend have determined that these polymers form a compatible blend, or a thermodynamically miscible pair, in all mixing combinations. The creation of hydrogen bonds between the – OH and C=O groups of PVA and PVP in their blend solution, resulting in a highly compatible solution cast blend film over the whole compositional ratio range [24]. In addition to biomedical applications, blends of PVA–PVP with various additives have been established as an advanced polymer composite matrix for a variety of technological and engineering applications, including electrical insulators [25], gas sensors [26], and optoelectronics devices [27].

The dielectric constant and the dissipation factor are two dielectric parameters, with the dielectric constant being the most generally employed to characterize the material's dielectric characterization. Changes in a dielectric material's characteristics as a function of temperature, and frequency give crucial information for understanding its relaxation behavior [16]. Electronic packaging is more appealing to low-conductivity-strength materials. Because of their flexibility, controlled dielectric permittivity, and superior dielectric breakdown strength, the resulting polymer-based composites are thought to be potential candidates for capacitors and charge-storage applications [28,29]. Electrolytes with better conductivity and chemical stability are needed to increase the performance of energy storage devices such as batteries, supercapacitors, solar cells, and fuel cells [30,31]. As a result, scientists are developing a novel polymer structure with increased ionic conductivity and mechanical stability. Polyvinyl alcohol, Polyvinyl pyrrolidone, Polyvinylidene fluoride, Polyethylene glycol, Polyvinylchloride, Polyacrylonitrile, and Polyvinyl sulfone are currently popular solid polymer

electrolyte materials (SPEs). Ionic conductivity and electrochemical stability are common transport features seen in SPEs [32,33].

Using a sol-gel process and a solution casting method, MgO NPS and PVA-PVP/MgO nanocomposite films were produced at varied weight ratios in the current work. Characterization methods such as X-ray diffraction (XRD) and scanning electron microscopy (SEM) were used to investigate the structural features of the samples. As a result, the optical, mechanical, dielectric, and electrical conductivity performance of varistors are investigated in this study.

2 Materials and Characterizations

2.1 Experimental Conditions Synthesis

2.1.1 Materials and films preparation

The source material and chelating agent utilized were magnesium acetate tetrahydrate ($Mg(CH_3{\cdot}COO)_2{\cdot}4H_2O$, MW = 214.45; Nova Oleochem Limited, India) and citric acid, $C_6H_8O_7$ (MW=192.124; LOBA Chemie, India). PVP/PVA films were prepared using PVA $[CH_2CH(OH)]_n$, (MW = 125000) from Alpha Chemica and PVP $[C_6H_9ON]_n$ (MW = 40000) from Research-lab Fine Chem. The MgO and nanocomposite films were made with double-distilled (DD) water as a solvent.

2.1.2. **Preparation of samples**

The following procedure was used to make MgO nanoparticles using the sol-gel technique. To begin, dissolve 5 g of high-grade Mg $(CH_3{\cdot}COO)_2.4H_2O$ and 5 g of Citric acid in 50 mL DD water for 2.0 hours with magnetic stirring. The resulting sol was baked for 12 hours at 80 ^oC, then cooled to 60 ^oC before stirring for another 45 minutes to get the gel. The gel was aged at room temperature for 15 hours (RT). Finally, MgO NPs were obtained by calcining the gel at 550 ^oC for 4.0 hours. The solution cast technique was used to make PVA/ PVP films with an 80 wt% PVA and 20 wt% PVP composition. 1.6 g PVA was dissolved in 60 mL DD water at 60 ^oC with continuous stirring until a clear and homogenous solution was formed. After that, 0.4 g PVP was dissolved in 40 mL DD water and mixed with the PVA solution at room temperature. We found that PVA/ PVP ratio of 80:20 produced more flexible and homogeneous films during the preparation procedure. The combined PVA/PVP solution was then agitated at room temperature for another 30 minutes. To avoid agglomeration, the needed masses (0.0, 0.06, 0.3, 0.6, 3.1 and 6.25 wt %) of MgO NPs were added to the PVA/ PVP solution under continuous stirring for 1.0 h at RT, then the solutions were mixed for 5 minutes with an ultrasonic at 110 watts. To verify that all solvent residues were eliminated, the finished mixture

was placed on Petri plates and dried for 4 days at 40ºC in the oven. In the host PVA/PVP polymeric blend, the wt % of MgO NPs is calculated as follows: $xwt.\% = \frac{w_d}{w_d+w_p}\ x\ 100\%$,

where w_d denotes the weight of the MgO NPs and w_p denotes the weight of the PVA/PVP polymeric blend.

2.2 Device Characterizations

To establish the polymeric nanocomposite crystallographic structure of the films, X-Ray patterns are documented using a diffractometer Lab XRD-6000 Shimadzu using Cuk_α Monochromatic radiation technique. The materials were examined using a scanning electron microscope (SEM) model (JSM-6360) that operated at 20 kV and used surface morphology. JASCO spectrophotometers V-570 at wavelengths between 190 and 2500 nm were used to test the absorbance $A(\lambda)$, and transmittance $T(\lambda)$ of investigated polymeric composite films in the UV–Vis and NIR regions. The AC electrical conductivity/dielectric characteristics were measured using an automated LCR meter (FLUKE-PM6306 Model). At different temperatures ranging from 30 ºC to 130 ºC, measurements were made in the frequency range of 100 Hz–1 MHz. Before the measurements, two copper plates were put between the samples as an ohmic contact. For PVA-PVP/ MgO polymeric nanocomposite films, the values of capacitance (C), resistance (R), and loss tangent ($tan\delta$) at each excitation frequency were measured. The nonlinear current (I)-voltage (V) relationship was also examined using the same device. Tensile testing was performed on PVA-PVP/MgO films to determine their mechanical properties. For stress-strain measurements, a tensile testing machine was employed (AMETEK, USA). The extending force was measured using a microprocessor-connected digital strength gauge (Hunter Spring ACCU Force II, 0.01 N, USA). A gearbox and a homemade engine connection were used to control the strain rate. The accuracy of the strain measurement was about 0.1 mm. Throughout the experiment, the elongation rate was kept at 6 mm/min.

3. Results and discussions

3.1. **XRD and SEM measurements**

XRD was used to evaluate the structural characteristics of the MgO NPs generated, as shown in Fig.1(a). The observed distinctive diffraction peaks in the MgO diffractogram are consistent with previous findings [6,23,34], which established the well-crystallized cubic MgO (periclase) structure of its nanoparticles. After calcination at 550 ºC, the XRD pattern of synthesized MgO contained 2θ values at 37.68º, 42.54º, and 62.64º,which matched to the (111), (200), and (220) planes, respectively (JCPDS Card No.45-0946). The existence of cubic MgO

(periclase) alone, with high crystallinity, was indicated by these strong diffraction peaks. These results are consistent with those of previous researchers [35] and indicate the purity of produced MgO NPs, as no peaks linked to Mg, $Mg(OH)_2$, or any other contaminants can be seen. The presence of prominent peaks implies crystalline MgO with a cubic structure (periclase). Scherer's formula [36] was used to determine the crystallite size (D) of MgO in nanometers:

$$D = \frac{k\lambda}{\beta \cos\theta} \quad \textbf{(1)}$$

where K is Scherer's constant, equals 0.9, λ is the X-ray source's wavelength, β is the half-maximum peak width (in radians), and θ is the angle of the corresponding peak (in radians). D had an average value of 30 nm.

Indeed, S. elgamal [23] used sol. gel to produce MgO nanoparticles and discovered that D = 14.29 nm. The solvent mixed spray pyrolysis process was used by Nemade and Waghuley [36] to synthesize MgO nanoparticles, and they discovered that D = 9.2 nm. Based on the XRD pattern observed for MgO NPs measuring 18.4 nm that were synthesized using the sol-gel process, Gh. Mohammed et al.[6] found $Mg(OH)_2$ in PVA/PVP blend

Fig. 1b shows the XRD patterns for the pure PVA-PVP (80%-20%) blend and blends including 0.06, 0.1, 0.3, 0.6, 3.1, and 6.25 wt% MgO NPs. The pure PVA–PVP blend (Fig. 1b) shows a diffraction peak at 19.68° and 40.55°, which is due to the PVA semi crystalline polymer [37]. This data demonstrates that there is a wide range of intermolecular hydrogen bonding between the functional groups (–OH···O=C) of PVA and PVP in their blend, resulting in massive destruction of PVA crystalline domains and a significant reduction in blend diffraction peak intensity. Furthermore, all the individual MgO peaks were absent from the composite, indicating the presence of polymer–nanoparticle interactions in the films. The average crystallite sizes D for nanocomposite films are estimated using Scherer's formula [36] Eq.1. Table 1 reveals that the average crystallite diameters D increase with increasing dopant concentrations, indicating a microstructural variation within the polymer matrix, indicating that PVA-PVP crystallites were ordered in nanocomposite films. The strain (ε), and dislocation density (δ) of the particles were calculated via the following formula and refining the data of the samples.

$$\epsilon = \frac{\beta \cos\theta}{4}, \quad \textbf{(2)}$$

$$\delta = \frac{1}{D^2} \quad \textbf{(3)}$$

With increased MgO NPs in the films, these parameters decrease, reflecting the minuscule size of MgO nanoparticles as shown in Table1. The inter-planar distance (d) was determined using Bragg's Eq.4 [38].

$$d = \frac{n\lambda}{2sin\theta}, \quad \textbf{(4)}$$

With increasing MgO loadings, the inter-planar distance is observed to be slightly affected. The findings are consistent with earlier researchs [6, 23,36].

The crystalline fraction (X_c) and its difference with dopant content is given in Table1 by using the relation[38].

$$\mathrm{X_C} = \frac{\mathrm{A_{crystalline}}}{\mathrm{A_{crystalline}} + \mathrm{KA_{amorphous}}}, \quad \textbf{(5)}$$

$A_{crystalline}$ and $A_{amorphous}$ are the areas of crystalline and amorphous halo reflections, respectively, and K is constant and equal to unity. Due to the development of dopant aggregates or clustering of MgO nanoparticles inside the (PVA-PVP) blend matrix, which enhances the amorphicity in the nanocomposites, the crystallinity of the polymer nanocomposites is clearly decreasing with the amount of MgO NPs, as shown in Table.1. Complex formation owing to interference clearly affects molecular mobility, resulting in molecular entanglement or a reduction in polymer crystallization. Non-crystalline areas with randomly folded polymer chains are related to these crystalline regions. As a result of the charge transfer, MgO nanoparticles can fill the interstitial spaces between the polymer chains and bind them via hydrogen bonds.

SEM is a valuable tool for determining how MgO NPs interact and distribute in polymer chains. Fig. 2a showed the spherical nano-MgO with a diameter of 35.75 nm; and uniform spherical nano-MgO agglomerated and stacked with each other [39]. Fig. 2(b)–(e) show photographs of the surface morphology of the MgO NPs dispersed blend nanocomposite film. A smooth, impurity-free surface characterizes pure blend film, as shown in Fig. 2(b). Fig. 2(c) shows that there are particles on the surface of the blend film with 0.6 wt% MgO NPs doping, indicating the presence of small interactions of MgO NPs with the chains, whereas higher MgO NPs percentages (3.1, and 6.25 wt %) reveal some agglomerated zones of MgO nanoparticles with a uniform and homogeneous distribution over the entire surface of the film. The presence of a hydroxyl group in the structure of nanocomposites, which is important for the attachment of MgO NPs to the polymer matrix and hence for the stability of the nanocomposites, causes the cluster size to rise as the concentration of MgO increases. When the number of MgO NPs increases, a big cluster forms, which affects the characteristics of the films, as seen in Fig. 2d and e. Thus, morphological investigations show that MgO NPs are well disseminated within the blend matrix, forming clusters, and no phase separation occurs [6,40].

3.2. Stress-strain behaviour of MgO/PVA-PVP polymeric films.

Mechanical factors play a major role in film quality and applicability. The stress-strain curves of MgO/PVA-PVP films at room temperature with a strain rate of $5x10^{-3}$ sec^{-1} are presented in Fig. 3. The computed mechanical properties of MgO/PVA-PVP polymeric nanocomposite films were exhibited in Table.2. The MgO content had a significant impact on the mechanical properties of composites. Fig. 3a shows common stress-strain curves. (PVA-PVP) films were flexible, with high elongation at break and low strength. The yield strength and tensile strength at break of MgO / (PVA-PVP) nanocomposite films rose significantly when the MgO content was increased [41,42]. As demonstrated in Fig. 3b, Young's modulus rose significantly as MgO increased. The MgO /(PVA-PVP) nanocomposite films had better tensile strength and elongation at break than pure (PVA-PVP) film, as illustrated in Fig. 3c. The tensile strength of the composite film with 6.25 wt % MgO rose from 5.92 MPa for neat (PVA-PVP) film to 10.65 MPa. With increasing MgO, however, the equivalent elongation at break of the MgO /(PVA-PVP) composite films increased[43,44]. These findings indicate that the MgO nanofillers provided significant reinforcement to the composite films. MgO, being an inorganic filler with a high modulus, can be employed as reinforcing nanofillers in polymeric composites [45]. The interactions between the filler and matrix might be greatly enhanced after effective (PVA-PVP) imbedding on MgO nanofillers, which would enable stress transfer under external strain.

3.3 The optical analysis of PVA–PVP /MgO polymeric nanocomposite films.

Fig. 4a displays the variation in absorbance for (PVA–PVP/MgO) nanocomposites as a function of the wavelength. The figure reveals that the absorbance of all nanocomposites samples raises in the UV region due to the excitement of electrons from the valance band to the conduction band at these energies, as well as the high absorbance of nanocomposites samples in the UV region due to the photon energy sufficient to interact with atoms. The varieties of potential electron transitions are decided by changes in transmitted and absorbed light. The essential absorbance spectra indicate the shift from one band to another [46,47]. Due to the insufficient energy of incoming photons to interrelate with atoms, the absorbance of nanocomposite samples is low in the near-infrared and visible ranges. The occurrence of an electronic transition from n to π^* coupled to a carbonyl bond (C = C) via the host polymer network results in a modest shoulder peak at 288.74 nm for all extant polymeric samples in the UV region [48]. Films doped with MgO showed an increase in absorption rate measured over the full spectrum. The increased absorption activity is a result of MgO NPs interacting with the

polymer network by forming new intermolecular bonds throughout the whole polymer backbone network via OH anions. This causes a modification as a result of additional defects, resulting in the development of new bandgap levels when the MgO -dopant concentration is increased [49]. Due to the establishment of intermolecular hydrogen bonds between Mg^{+2} ions and the adjacent OH groups of the PVA and PVP major chains, the absorption band changes. Because the gap between the valence and conduction bands is greater in the polymer blend, it has a low absorbance [47]. The absorption of the (PVA–PVP) blend rises as the number of MgO NPs increases. As shown in Fig. 4a, the rise in absorption values for polymer films with higher MgO concentrations from 0.06 wt% to 6.25 wt% coincides with a decrease in transmittance values. As demonstrated in Figs. 4 a&b, the absorbance increases and the transmittance reduces as the concentration of MgO NPs increases. This is due to the accumulation of nanoparticles as the number of charge carriers and concentration increases [6]. The optical absorption spectra are a major source of determination the optical band gap energy in crystalline and amorphous materials. The principal absorption corresponding to the excitation of an electron from the valence band to the conduction band may be utilized to estimate the optical bandgap value. The samples bandgap, E_g, may be determined using Tauc's question [50]:

$$\alpha h\upsilon = B(h\upsilon - E_g)^m \ , \qquad \textbf{(6)}$$

where B, $h\upsilon$, and E_g are constant, photon energy, and optical energy gap, respectively. α is the absorption coefficient considered using the formula [47]: $\alpha = 2.303\frac{Abs.}{t}$, where t is the thickness of the film and m = *1/2* for direct and *2* for indirect allowed transitions. To determine the transitions and define the band edges, which includes graphing $(\alpha h\upsilon)^{1/2}$ and $(\alpha h\upsilon)^2$ values with respect to $(h\upsilon)$ values presented in Fig. 5. (a,b). Table 3 shows the results of extending the linear component of the plots 5(a &b). Because of the development of energy levels with increasing the doping contents in the films, the $E_{g(ind)}$ (indirect bandgap) and E_{gd} (direct bandgap) of the films were lowered from 4.83 eV to 4.02 eV . and from 5.26 to 4.96 for $E_{g(ind)}$ and E_{gd}, respectively. [6, 46,51]. Due to the interaction of PVA-PVP chains and $(Mg)^{+2}$ -ion contents, these defects are the primary source of charge transfer complex (CTC)-generation complex charging. These defects are responsible for the bandgap localized states, which correspond to disorder levels in expanded samples. PVA -PVP/ MgO [6], (PVA–MgO–SiC) nanocomposites [46], and PVA- PEO/ MgO [51], polymeric nanocomposite films have all demonstrated this behavior. The rise in density of localized states in the bandgap is related to the generation of new energy levels (traps) from the HOMO to the LOMO, resulting in a

reduction in E_g values. The absorbance values in Fig. 4a was used to compute the absorption edge energy E_a values for these films. Tauc's Eq. (7) used to calculate the $E_{g(T)}$ values of photon-absorbing materials [52].

$$\omega^2 A = (h\omega - E_g)^2 \quad \textbf{(7)}$$

The angular frequency of photons incident is equal to $2\pi\nu = 2\pi c/\lambda$, while λ is the wavelength of photons incident at velocity c is equal to ω. For these films, Tauc's plot ($A^{1/2}/\lambda$ versus $1/\lambda$) was used, see Fig 6a. Extrapolating these line segments of the curves to determine band gap λ_g using the following relation yielded the values of $E_{og(T)}$:

$$E_{g(T)} = hc/\lambda_g \quad (8)$$

The estimated $E_{g(T)}$ values of the PNC are also shown in Table 3. This $E_{g(T)}$ values are seen to be in the middle of the E_{gd} and E_{gind} values for these PNC.

The extended tail for decreasing photon energy below the band edge may be expressed in absorption spectra by[53]

$$\alpha = \alpha_o e^{\frac{h\nu}{E_U}}, \quad \textbf{(9)}$$

where α_o is the constant, $(h\nu)$ is the photon energy, and (E_U) is the Urbach's energy, which would be the width of the band tails for localized states in the bandgap. As illustrated in Fig. 6b, the E_U values were computed by taking the reciprocal gradient of the linear parts of the ln(α) against hυ plot (6b). As the amount of MgO nanoparticles increased, the E_U values raised from 1.015 eV to 3.58 eV. This finding supports the XRD findings, which show that E_U is caused by the material disorder, which leads to the tail in the valence and conduction bands [54].

3.4. Complex permittivity spectra and dielectric polarization behavior

Eqs. (10&11) were used to calculate the real ε_1 and dielectric loss ε_2 parts of the complex permittivity $\varepsilon^* = \varepsilon_1 - j\varepsilon_2$ for PNC films as a function of frequency[55];

$$\varepsilon_1 = \frac{C_p t}{\varepsilon_o a}, \quad \textbf{(10)}$$

$$\varepsilon_2 = \varepsilon_1 tan\delta, \quad \textbf{(11)}$$

The capacitance, sample thickness, free space permittivity, and pellets area are represented by C_p, t, ε_o, and A, respectively. Fig. 7 shows the spectra of complex dielectric permittivity (ε_1 and ε_2) and dielectric loss tangent $\tan\delta$, $\tan\delta = \varepsilon_2/\varepsilon_1$ of (PVA–PVP)–MgO films at 30 ºC, as well as (PVA–PVP)/ 6.25 wt %MgO films with temperature variation. These spectra show that the ε_1 values of PNC films reduce as frequency increases, which is a frequent feature of

PNC materials [54-56]. The ε_1 values of these materials nonlinearly decline with the rise in frequency from 100 Hz to about 100 kHz, and then slowly approach a steady-state value near 1 MHz, as shown in Fig. 7a. With the rise in frequency in the lower-frequency range (i.e. 100 Hz–1 kHz), a sharp decrease in $\varepsilon_1$values have been observed. Fig.7a indicates that when the frequency of the alternating field rises, the proportionate increase in ε_1 values of PNC films decreases. Interfacial polarization (IP), also known as Maxwell–Wagner–Sillar (MWS) polarization process [24]. The IP effect cannot synchronize with fast reversible changes in the ac field at higher frequencies [24,55], so its contribution to dielectric polarization is negligible, and the observed ε_1 values are primarily ascribed to the dipolar reorientation and electronic polarization processes of these films. The dielectric dispersion of PVA-PEG-PVP-MgO films [57] and the PVA/PVP blend matrix-based nanocomposite films [16] are similar to these findings. The MWS effect refers to the build-up of charges at the interfaces of distinct permittivity and conductivity elements of composite dielectric material, resulting in the development of micro capacitors across the material's volume. Due to the large contribution of such micro capacitors to dielectric polarization, there is a rise in ε_1 values at low frequencies, The frequency dependent ε_1 values of nanocomposite material are also governed by the dipolar sizes, density, and arrangement of these dipoles, in addition to the MWS contribution. The drop in $\varepsilon_1$value with increasing frequency in PNCs can also be related to the rate of dipole orientation in the direction of a time-varying applied electric field [58,59].

The dipolar groups in solid polymer dielectrics can orient themselves in the direction of low-frequency electric fields, but it becomes more difficult for larger dipolar groups to orient themselves with the relatively fast time-varying electric fields of higher frequencies, and thus the ε_1 values of such materials decrease sharply as the frequency in the low-frequency region increases. This might be one of the reasons for a significant fall in ε_1 values of the (PVA–PVP)/MgO films as frequency increases. There is a steady and very tiny drop in the ε_1 values of the examined PNC nanodielectrics in the frequency area (f >100 kHz), and their $\varepsilon_2$values exhibit a slight alteration over the same frequency range (see inset of Fig. 7a). The PVA–PVP blend films frequency dependent ε_1 and ε_2 values were obtained to be in accord with previously published results [58,59].

In comparison to the pure PVA–PVP blend film, the ε_1 and ε_2 and $\tan\delta$ values of MgO dispersed in these PNC films are high across the whole frequency range (see Fig. 7b). It might be because MgO has a higher permittivity than PVA- PVP film. Furthermore, the current study shows that when the MgO nanoparticles are dispersed in the PVA–PVP blend matrix, the increase in ε_2 values of the pure PVA–PVP blend is relatively low compared to the MgO NPs

incorporated PNC films at low frequencies, implying that the contribution of MWS polarization effect increases. Previous dielectric investigations on pure PVA films [24, 58] and PVP films [60] show that there is no indication of any relaxation process in these films that can be evaluated in the frequency range 100 Hz–1 MHz. In the experimental frequency range of 100 Hz–1 MHz at 30 °C, the ε_2 and $\tan\delta$ spectra of the pure PVA–PVP blend, as well as the MgO dispersed PNC films of this blend (Fig. 7a), show no dielectric relaxation peak.

The ε_1 and ε_2 values of the PNC films were plotted versus wt % MgO, at fixed frequencies, in Fig. 8a to obtain insight into their MgO concentration-dependent behavior. The dispersion of MgO in the PVA–PVP blend increases the ε_1 values by a significant amount. This relationship between PNC film ε_1 and ε_2 values and MgO concentration suggests that when MgO NPs engage with the PVA–PVP structure, parallel dipolar ordering of the –OH and C=O functional groups is considerably enhanced. As a result, these findings suggest that loading MgO NPs into PVA–PVP blend matrix (80/20 wt%) can provide the best tunable dielectric properties and can be used as low loss nanocomposite materials.

The temperature-dependent dielectric behavior of a PNC film containing 6.25 wt% MgO was examined. At temperatures of 30, 50, 70, 90, 110 and 130 °C, the ε_1 and ε_2 and tanδ spectra of (PVA–PVP)–6.25 wt % MgO film are shown in Fig. 8b. The frequency dependent ε_1 values in the low and high-frequency areas, respectively, show non-linear and linear dispersion. Furthermore, when the frequency of the ac field decreases, the ε_1 values increase with the increase in temperature across the whole frequency range, and this increase enhances. The thermally induced dielectric polarization behavior of the PNC film is confirmed by its increase in permittivity as the temperature rises. As the temperature rises, more free volume is created in the flexible solid dielectric matrix, promoting parallel dipolar re-ordering and therefore increasing dielectric polarization in polymeric dielectric materials. [55, 56]. These findings further support the PNC films temperature-tunable dielectric characteristics in the 30–110 °C temperature range.

The real and imaginary parts of the electric modulus spectra $M^*(\omega)$ can be obtained from the complex permittivity $\varepsilon^*(\omega)$ using the relation[55,59] $M^* = M' + iM''$, $M^* = \frac{1}{\varepsilon^*} = \frac{\varepsilon'}{\varepsilon'^2+\varepsilon''^2} + i\frac{\varepsilon''}{\varepsilon'^2+\varepsilon''^2}$, where M' and M'' are the real and imaginary parts of the electric modulus, respectively. After removing the contributions of the electrode polarization (*EP*) effect, electrode-dielectric contact, electrode material, and adsorbed impurity effects from the total polarization of a material, the $M^*(\omega)$ spectra are well suited for analyzing the bulk properties of composite dielectric material [55]. At 30 °C, the electric modulus of (PVA–PVP) /MgO nanocomposites is shown by the real part M' (ω) and loss part M'' (ω) spectra in Fig. 9a.

In the lower frequency range, the M' values of these PNC materials quickly rise with increasing frequency, whilst the M'' spectra reveal a relaxation peak assigned to the MWS relaxation process [61,62], which was not seen in the M" spectra of a pure blend of PVA – PVP film [61,62]. Only one relaxation peak is detected in this investigation, which may be attributed to either the MWS relaxation process or the PVA and PVP main chains cooperative mode motion (α-relaxation) caused by the miscible blend. Because the modulus spectra of pristine PVA do not exhibit such relaxation in the experimental frequency range [63], the relaxation peak in the M'' spectra of PVA–PVP blend may be attributed to the MWS process, but there is also a high probability that this peak is due to the existence of α-relaxation, as these two mechanisms have been observed superimposed on each other in PNC materials [64]. The primary goal of this research is to see how MgO concentration affects the dielectric and electrical properties of organic-inorganic composites. Essentially, several types of micro-environments are formed in the PVA–PVP blend matrix, which are related to hydrogen bonding between the PVA–PVA chains in the crystalline and amorphous phases, and the PVA–PVP chains in the amorphous phase, as well as at the amorphous–crystalline interface [60]. The accumulation of charges at these interfaces supports the observed M'' peak, which corresponds to the MWS relaxation process.

In addition, the MWS process is expected to take place owing to the existence of MgO nanofiller in the PNC films. In addition, because the mobility of charges accumulated at heterogeneous interfaces is influenced by polymer chain segmental motion, the MWS relaxation process is influenced by polymer chain dynamics. In comparison to the pristine PVA–PVP blend film, Fig. 9a shows that the MWS relaxation peak of MgO dispersed PNCs shifts to the high-frequency side. The presence of inorganic nanofiller in the polymer matrix enhances MWS dynamics [24]. Fig. 9b shows the M' and M'' spectra of (PVA–PVP)–6.25wt% MgO film at several temperatures. The M' values of the PNC film decline with increasing temperature at a fixed frequency, as shown in the figure, whereas the M'' values of the PNC film increase with increasing temperature at variable frequency "As the temperature of the film increases, the intensity of the MWS relaxation peak increases and gradually shifts towards the high-frequency side, which is a common distinctive of polymeric nanocomposites [58].

AC and DC electrical conductivities

The nature of ion dynamics can be accurately obtained based on the well-known universal power low of Jonscher by calculating the frequency exponent(s) as follows [55]:

$$\sigma_{ac}(\omega) = \sigma_{total.ac}(\omega) - \sigma_{dc}(\omega = 0), \quad \textbf{(12)}$$

$$\sigma_{ac}(\omega) = B\omega^{S}, \quad \textbf{(13)}$$

where ω, *t, B, s* and σ_{dc} are the angular frequency, the thickness of films, constant, the frequency exponent, and the DC conductivity of the polymeric films.

Fig. 10 (a&b) depicts the (ac) electrical conductivity $\sigma_{ac}(\omega)$spectra of PVA-PVP-/ MgO films at 30 °C and the PVA-PVP-6.25 wt % MgO film with temperature change. The σ_{ac} value of the PVA-PVP film is on the order of 10^{-9} S/ m at 100 Hz, as revealed in Fig. 10a, and there is a two-order-of-magnitude increase at the same frequency when 6.25 wt % MgO is dispersed in the PVA-PVP matrix. When the temperature of the PVA-PVP -6.25 wt% MgO film is increased from 30 to 130 °C, the σ_{ac} values increase by nearly one order of magnitude (Fig. 6b). Furthermore, the σ_{ac} values improve at a rather high pace with increasing frequency up to around 100 kHz, after which the rate of increase slows down. The semicrystalline structure of the host matrix causes conductivity dispersion in PVA-PVP matrix-based PNC films, as previously observed [24,55]. Due to the polymer–nanoparticle electrostatic interactions, a rise in the number of free charges and/or the development of some beneficial charge conductive paths is revealed by the enhancement of these materials σ_{ac} values.

The linear fit of low-frequency σ_{ac} data for electronic conduction (σ_{dc}) and the power law fit $\sigma_{ac}(\omega) = \sigma_{dc} + A\omega^{s}$ of high-frequency σ_{ac} data were used to estimate the direct current (dc) electrical conductivity σ_{dc} of these materials and s values for the PVA-PVP -*6.25* wt% MgO films with its temperature variation (see Table 4). The σ_{dc} values rise as the temperature of the PNC film rises, as can be seen from this table. The s values of the polymeric films were noticed to be less than unity (s = 0.78, 0.71, 0.66, 0.64, 0.56, and 0.48 at 30, 50, 70, 90, 110, and 130 °C, respectively), indicating that charge transport in these composite materials takes place via the correlated barrier hopping (CBH) model, which is a common feature of disordered materials [24].

Fig. 10c depicts the Arrhenius behavior of the temperature-dependent σ_{dc} values of the (PVA–PVP)–6.25 wt % MgO film. Using the relationship, $\sigma_{dc} = \sigma_o \exp(^{E_\sigma}/_{k_B T})$, where σ_o, k_B and T are a pre-exponent factor, Boltzmann's constant in eV (8.617×10^{-5} eV K^{-1}) , and the temperature in absolute scale, respectively. The conductivity activation energy E_σ of the PNC film was calculated from the slopes of the Arrhenius plot. The determined E_σ value of 0.517 eV emphasis the hopping conduction mechanism for a.c. conduction for all samples due to the comparatively low values of E_σ. [24, 58, 59], so the examined PNC materials might be used as a basic matrix in the creation of nanocomposite solid polymer Electrolytes (SPE) materials due to their low E_σ value [24].

3.5. *I–V* characteristic curve of PVA -PVP/ MgO nanocomposites.

In order to protect electronic circuits and equipment from overvoltage, nonlinear resistors (varistors) based on nanocomposite polymeric materials are often utilized. This type of device promotes two objectives: the first is to better understand the electrical behavior of nanostructure composite devices, and the second is to apply the investigated resultant behavior of the fabricated device to electrical circuits like power saving, power limiting, and voltage level stabilizer domains. A novel material based on a polymer with a low threshold voltage and a larger value of ρ is needed nowadays [63]. The adaptive mobility of charge carriers that develop by doping may be used to derive the conductivity type of polymeric materials. The mobility of charge carriers that develop through doping (negative or positive) leads to electric charge over the chains of polymer which causes the electronic conductivity of polymers. The conductivity was observed to increase depending on the mobility of the carriers [65]. At room temperature, Fig. 11(a&b) shows the current (*I*) flowing through the PVA-PVP and its MgO nanocomposites versus the applied voltage (*V*). The corresponding electric current increases when the applied potential difference arises. Furthermore, as the MgO-contents increase, so do the current values. The *I-V* characteristics of the films at low applied voltage (*V*) follow Ohm's law. There is an increase in current (*I*) in the doped samples as the applied voltage (*V*) is increased, which starts slowly and then accelerates.

The coefficient (ρ), which measures the nonlinearity of varistors, may be calculated using the following expression [66]:

$$\rho = \frac{d(\ lnI)}{d(lnV)} \qquad \textbf{(14)}$$

If ρ is equal to one, the material exhibits linear behavior or ohmic conduction. Most PNCs, according to the literature, act nonlinearly [23, 67]. Fig.11 (c&d) displays the relationship between the *ln I* and *ln V*, which was used to analyze nonlinearity in the films studied. As is clear, ρ is the slope of these lines, and their values are presented in Table 5, ranging from 0.5 to 1.63, supporting the nonlinearity behavior. By adding additional MgO NPs, the ρ value rises. As shown in Fig.11 (c&d), loading MgO NPs raises *I* values.

The I–V characteristics' nonlinear performance was noticed and may be explained by two factors. To begin with, when the applied voltage exceeds the nominal voltage (or breakdown voltage), the material's resistance drops sharply, causing an increase in conductance and current above the 100 V threshold that controls the barrier height and allows more charges to jump between levels than the current flow across the junction, resulting in increased current values. The second explanation is that the additional MgO content forms physical contact networks

within the polymer matrix, which could result in an increase in the current [23]. Another important consideration is that the addition of MgO creates localized traps in the energy bandgap, resulting in a decrease in E_g and an increase in current. As a result, the bandgap between the valence band and the conduction band is greatly decreased, making it easier for electrons to jump from the valence band to the conduction band. The polar O^{-2} terminated MgO NPs contributes significantly to the increase in current, so, MgO NPs have the potential to form "charge transfer complexes (*CTCs*)," which lower the barrier height between trapping sites [68]. These CTCs promote polarization and hence charge mobility, resulting in an increase in *I*. This behavior suggests that the existing flexible films with a high MgO NPs content might be useful as nanocomposite materials in a varistor device. This behavior is consistent with that observed in PVA-PVP doped with Mg ions.

4 | Conclusions

This paper reports on the structural, morphological, optical, mechanical, dielectric, and electrical characteristics of (PVA–PVP)–x wt% MgO polymeric nanocomposite films. Because of the high miscibility of the PVA–PVP blend (80/20 wt%), these films are largely amorphous, and there is an enhancement in polymer–nanoparticle interactions as the MgO level in the films rises. With increasing MgO concentration, the optical energy bandgap (direct and indirect) of these PNC films decreases, whilst the films' absorbance (optical density) rises. The Urbach's tail energy grows dramatically as the MgO content in the PNC films increases. The tensile strength increased by 100%, while Young's modulus increased by 300%, revealing that the (PVA–PVP) blend and MgO NPs successfully complexed and interacted. The temperature-dependent dielectric and electrical investigation of the (PVA–PVP)–6.25 wt% MgO film verifies the Arrhenius behavior of dielectric relaxation and electrical conductivity, as well as a linear rise in dielectric permittivity across the temperature range 30–130 °C. The PNC film has substantially lower activation energy than unity. Nonlinear behavior in the I-V curve observed in films with greater dopant content of MgO NPs. The multifunctional characteristics of these MgO dispersed high-performance PNC materials verify their practicability as potential candidates for next-generation flexible optoelectronics, gas sensors, base matrix for ion-conducting nanocomposite solid polymer electrolytes, and electrical insulator for microelectronic devices, as evidenced by the structural, morphological, optical, dielectric, and mechanical properties.

Data availability

All data generated or analyzed during this study are included in this published article.

Declarations

Conflict of interest

The authors declare no conflict of interests.

References

[1] H. Hu, F. Zhang, S. Luo, W. Chang, J. Yue, C. Wang, Recent advances in rational design of polymer nanocomposite dielectrics for energy storage, Nano Energy 74 (2020), 104844. [2] Y. Guo, X. Zuo, Y. Xue, J. Tang, M. Gouzman, Y. Fang, Y. Zhou, L. Wang, Y. Yu, M. H. Rafailovich, Engineering thermally and electrically conductive biodegradable polymer nanocomposites, Compos. B Eng. 189 (2020), 107905.

[3] S. Fu, Z. Sun, P. Huang, Y. Li, N. Hu, Some basic aspects of polymer nanocomposites: a critical review, Nano Mater.Sci. 1 (2019) 2–30.

[4] P. Bose, D. Deb, S. Bhattacharya, Lithium-polymer battery with ionic liquid tethered nanoparticles incorporated P(VDF-HFP) nanocomposite gel polymer electrolyte, Electrochim. Acta 319 (2019) 753–765.

[5] S. Mallakpour, N. Nouruzi, Effect of modified ZnO nanoparticles with biosafe molecule on the morphology and physiochemical properties of novel polycaprolactone nanocomposites, Polymer 89 (2016) 94–101.

[6] Gh. Mohammed, Adel M. El Sayed, W.M. Morsi. Spectroscopic, thermal, and electrical properties of MgO/ polyvinyl pyrrolidone/ polyvinyl alcohol nanocomposites, Journal of Physics and Chemistry of Solids 115 (2018) 238–247. https://doi.org/10.1016/j.jpcs.2017.12.050

[7] R.T. De Silva, M.M.M.G.P.G. Mantilaka, S.P. Ratnayake, G.A.J. Amaratunga, K.M. Nalin de Silva, Nano-MgO reinforced chitosan nanocomposites for high performance packaging applications with improved mechanical, thermal and barrier properties, Carbohydr. Polym. 157 (2017) 739–747.

[8] R. Halder, S. Bandyopadhyay, Synthesis and optical properties of anion deficient nano MgO, J. Alloy. Comp. 693 (2017) 534–542.

[9] L. Chen, P. Bai, W. Li, Preparation of a novel magnesium oxide nanofilm of honeycomb-like structure and investigation of its properties, Chem. Eng. J. 303 (2016) 588–595.

[10] N.M.A. Hadia, H.A. Mohamed, Characteristics and optical properties of MgO nanowires synthesized by solvothermal method, Mater. Sci. Semicond. Process. 29 (2015) 238–244.
[11] X. Meng, Z. Liu, C. Deng, M. Zhu, D. Wang, K. Li, Y. Deng, M. Jiang, Microporous nano-MgO/diatomite ceramic membrane with high positive surface charge for tetracycline removal, J. Hazard Mater. 320 (2016) 495–503.
[12] M.Y. Nassar, T.Y. Mohamed, I.S. Ahmed, I. Samir, MgO nanostructure via a sol-gel combustion synthesis method using different fuels: an efficient nano-adsorbent for the removal of some anionic textile dyes, J. Mol. Liq. 225 (2017) 730–740.
[13] S. Demirci, B. €Oztürk, S. Yildirim, F. Bakal, M. Erol, O. Sancako_glu, R. Yigit, E. Celik, T. Batar, Synthesis and comparison of the photocatalytic activities of flame spray pyrolysis and sol–gel derived magnesium oxide nano-scale particles, Mater. Sci.
Semicond. Process. 34 (2015) 154–161.
[14] M. Li, X. Wang, H. Li, H. Di, X. Wu, C. Fang, B. Yang, Preparation of photoluminescent single crystalline MgO nanobelts by DC arc plasma jet CVD, Appl.
Surf. Sci. 274 (2013) 188–194.
[15] F. Wang, N. Ta, W. Shen, MgO nanosheets, nanodisks, and nanofibers for the Meerwein–Ponndorf–Verley reaction, Appl. Catal. 475 (2014) 76–81.
[16] V. Siva, D. Vanitha, A. Murugan, A. Shameem, S. Asath Bahadur. Studies on structural and dielectric behaviour of PVA/PVP/ SnO nanocomposites, Composites Communications 23 (2021) 100597, https://doi.org/10.1016/j.coco.2020.100597
[17] Ayoub Moghadam, Mohammad Salmani Mobarakeh, Mohsen Safaei, Samira Kariminia.. Synthesis and characterization of novel bio-nanocomposite of polyvinyl alcohol-Arabic gum-magnesium oxide via direct blending method, Carbohydrate Polymers 260 (2021) 117802. , https://doi.org/10.1016/j.carbpol.2021.117802
[18] A.M. Elbarbary, M.M. Ghobashy, Controlled release fertilizers using superabsorbent hydrogel prepared by gamma radiation, Radiochim. Acta 105 (10) (2017) 865–876, https://doi.org/10.1515/ract-2016-2679.
[19] R. Alipour, A. Khorshidi, A.F. Shojaei, F. Mashayekhi, M.J.M. Moghaddam, Skin wound healing acceleration by Ag nanoparticles embedded in PVA/PVP/Pectin/ Mafenide acetate composite nanofibers, Polym. Test. 79 (2019), 106022.
[20] S.S. Shahrabi, J. Barzin, P. Shokrollahi, Blood cell separation by novel PET/PVP blend electrospun membranes, Polym. Test. 66 (2018) 94–104.
[21] M.T. Ramesan, V.K. Athira, P. Jayakrishnan, C. Gopinathan, Preparation, characterization, electrical and antibacterial properties of sericin/poly (vinyl alcohol)/poly

(vinyl pyrrolidone) composites, J. Appl. Polym. Sci. 133 (24) (2016) 43535, https://doi.org/10.1002/app.43535.

[22] Y. Zheng, Y. Liu, A. Wang, Fast removal of ammonium ion using a hydrogel optimized with response surface methodology, Chem. Eng. J. 171 (3) (2011) 1201–1208.

[23] S. El-Gamal, M. Elsayed . Positron annihilation and electrical studies on the influence of loading magnesia nanoribbons on PVA-PVP blend, Polymer Testing 89 (2020) 106681, https://doi.org/10.1016/j.polymertesting.2020.106681

[24] S. Choudhary, R.J. Sengwa, ZnO nanoparticles dispersed PVA–PVP blend matrix based high performance flexible nanodielectrics for multifunctional microelectronic devices, *Current Applied Physics* (2018), doi: 10.1016/j.cap.2018.05.023.

[25] Q. Wei, Y. Zhang, Y. Wang, W. Chai, M. Yang, Measurement and modeling of the effect of composition ratios on the properties of poly(vinyl alcohol)/poly(vinyl pyrrolidone) membranes. Mater. Des. 103 (2016) 249–258.

[26] R.J. Sengwa, S. Choudhary, S. Sankhla, Dielectric spectroscopy of hydrophilic polymers–montmorillonite clay nanocomposite aqueous colloidal suspension. Colloids Surf. A: Physicochem. Eng. Aspects 336 (2009) 79–87.

[27] N. Rajeswari, S. Selvasekarapandian, S. Karthikeyan, M. Prabu, G. Hirankumar, H. Nithya, C. Sanjeeviraja, Conductivity and dielectric properties of polyvinyl alcohol–polyvinylpyrrolidone poly blend film using non-aqueous medium. J. Non-Cryst. Solids 357 (2011) 3751–3756.

[28] O.S. Yakovenko, L.Y. Matzui, L.L. Vovchenko, V.V. Oliynyk, V.L. Launetz, A. V. Trukhanov, Dielectric properties of composite materials containing aligned carbon nanotubes, Inorg. Mater. 52 (2016) 1198–1203.

[29] X. Ding, S. Ahmed, N. Bao, J. Ding, R. Liu, J. Yi, Clustering-induced high magnetization in Co-doped TiO2, Emergent Mater 2 (2019) 295–301.

[30] K.O. Cooke, T.L. Khan, Effect of thermal processing on the tribology of nanocrystalline Ni/TiO2 coatings, Emergent Mater 1 (3–4) (2018) 165–173.

[31] Z. Xu, X. Chu, Y. Wang, H. Zhang, W. Yang, Three-dimensional polymer networks for solid-state electrochemical energy storage, Chem. Eng. J. 391 (2020), 123548.

[32] A. Hadi, A. Hashim, Y. Al-Khafaji, Structural, optical and electrical properties of PVA/PEO/SnO_2 new nanocomposites for flexible devices, Trans. Electr. Electron. 21 (2020) 283–292.

[33] A. Hashim, I.R. Agool, K.J. Kadhim, Novel of (polymer blend-Fe3O4) magnetic nanocomposites: preparation and characterization for thermal energy storage and release, gamma ray shielding, antibacterial activity and humidity sensors applications, J. Mater. Sci. Mater. Electron. 29 (12) (2018) 10369–10394.

[34] De Silva, RT., Mantilaka, MMMGPG., Ratnayake, SP., Amaratunga, GAJ., & Nalin de Silva, K.M., Nano-MgO reinforced chitosan nanocomposites for high performance packaging applications with improved mechanical, thermal and barrier properties. *Carbohydrate Polymers, 2016*, http://dx.doi.org/10.1016/j.carbpol.2016.10.038

[35] Wurood Abdulkhaleq Khaleela, Sinan Abdulhameed Sadeqb, I.A.M. Alanic, M.H.M. Ahmed .Magnesium oxide (MgO) thin film as saturable absorber for passively mode locked erbium-doped fiber laser, Optics and Laser Technology 115 (2019) 331–336, https://doi.org/10.1016/j.optlastec.2019.02.042

[36] K.R. Nemade, S.A. Waghuley, Synthesis of MgO nanoparticles by solvent mixed spray pyrolysis technique for optical investigation, Int. J. Metals (2014), https:// doi.org/10.1155/2014/389416, 2014.

[37] B.D. Cullity, S.R. Stock, Elements of X-Ray Diffraction, third ed., Prentice hall, New Jersey, 2001.

[38] I.S. Yahia, M.I. Mohammed, A. M. Nawar. Multifunction applications of TiO_2/poly(vinyl alcohol) nanocomposites for laser attenuation applications, Physica B:Condensed Matter 556, 48–60 (2019). https://doi.org/ 10.1016/j.physb.2018.12.031.

[39] Yuxun Ye, Yanming Liu, Tao Shi, Zhuojun Hu, Lei Zhong, Haobo Wang and Yaohui Chen. Effect of Nano-Magnesium Oxide on the Expansion Performance and Hydration Process of Cement-Based Materials, Materials 2021, 14, 3766. https://doi.org/10.3390/ma14133766

[40] Yasmin Khairy, H. I. Elsaeedy, M. I. Mohammed, H. Y. Zahran, I. S. Yahia. Anomalous behaviour of the electrical properties for PVA/ TiO_2 nanocomposite polymeric films, Polymer Bulletin https://doi.org/10.1007/s00289-019-03028-y

[41] Di Liu, Li Yuan, Hongyue Xu, Huafeng Tian , Aimin Xiang. PVA Grafted POSS Hybrid for High Performance Polyvinyl Alcohol Films with Enhanced Thermal, Hydrophobic and Mechanical Properties, POLYMER COMPOSITES—2019, DOI 10.1002/pc.25084

[42] A. Y. Yassin, Dielectric spectroscopy characterization of relaxation in composite based on (PVA–PVP) blend for nickel–cadmium batteries, J Mater Sci: Mater Electron (2020) 31:19447–19463, https://doi.org/10.1007/s10854-020-04478-1

[43] K. Rajesh, V. Crasta, N.B. Rithin Kumar, G. Shetty, P.D. Rekha, Structural, optical, mechanical and dielectric properties of titanium dioxide doped PVA/PVP nanocomposite. J. Polym. Res. 26, 99 (2019). https://doi.org/10.1007/s10965-019-1762-0

[44] S. Zhang, Y. Zhai, Z. Zhang, Preparation and properties of polyvinyl alcohol (PVA)/polyvinyl pyrrolidone (PVP) hydrogel. Appl. Mech. Mater. 84–85, 485–488 (2011). https://doi.org/10.4028/www.scientific.net/AMM.84-85.485

[45] R. S. Mahmood, S. A. Salman, N. A. Bakr.. The electrical and mechanical properties of cadmium chloride reinforced, PVA:PVP blend, Papers in Physics, vol. 12, art. 120006 (2020) , DOI: https://doi.org/10.4279/PIP.120006

[46] Hind Ahmed, Hayder M. Abduljalil, Ahmed Hashim. Structural, Optical and Electronic Properties of Novel (PVA–MgO)/SiC Nanocomposites Films for Humidity Sensors, Transactions on Electrical and Electronic Materials (2019) 20:218–232 https://doi.org/10.1007/s42341-019-00111-z

[47] A.M. Ismail, M.I. Mohammed and E.G. El-Metwally. Influence of Gamma irradiation on the structural and optical characteristics of Li-ion doped PVA/PVP solid polymer electrolytes. Indian Journal of Physics, 93, 2, 175-183 (2018).

[48] A.A. Alhazime, M.B. Mohamed, M.H. Abdel-Kader, J. Inorg. Organomet. Polym. Mater. 29(2), 436–443 (2019)

[49] I. S. Yahia, M. I. Mohammed, Facile synthesis of graphene oxide/PVA nanocomposites for laser optical limiting: Band gap analysis and dielectric constants, J. Mater. Sci.: Mater. Electron. 29, 8555–8563, (2018). https://doi.org/ 10.1007/s10854-018-8869-7.

[50] J. Tauc, Amorphous and Liquid Semiconductors, Plenum Press, London, New York, 1974, p. 171.

[51] Qayssar M. Jebur, Ahmed Hashim, Majeed A. Habeeb. Structural, Electrical and Optical Properties for (Polyvinyl Alcohol–Polyethylene Oxide–Magnesium Oxide) Nanocomposites for Optoelectronics Applications, Transactions on Electrical and Electronic Materials (2019) 20:334–343https://doi.org/10.1007/s42341-019-00121-x

[52] D.A. Davis, J.S. Shalliday, Some optical properties of cadmium telluride. Phys. Rev.118 (1960) 1020–1022.

[53] E.A. Davis, N.F. Mott, Conduction in non-crystalline systems V. Conductivity, optical absorption and photoconductivity in amorphous semiconductors. Philos. Mag. 22 (1970) 0903–0922.

[54] Mohammed, M.I., Khafagy, R.M., Hussien, M.S.A. et al. Enhancing the structural, optical, electrical, properties and photocatalytic applications of ZnO/PMMA nanocomposite membranes: towards multifunctional membranes. J Mater Sci: Mater Electron (2021). https://doi.org/10.1007/s10854-021-07402-3.

[55] M.I. Mohammed, Dielectric dispersion and relaxations in (PMMA/PVDF)/ZnO nanocomposites. Polym. Bull. (2021).https://doi.org/10.1007/s00289-021-03606-z

[56] N. Sabry, M.I. Mohammed, I.S. Yahia, Optical analysis, optical limiting and electrical properties of novel PbI_2/ PVA polymeric nanocomposite films for electronic optoelectronic applications. Mater. Res. Express **6**, 115339 (2019). https ://doi. org/10.1088/2053-1591/ab4c24.

[57] Ibrahim R. Agool, Majeed Ali, Ahmed Hashim. The Dielectric Properties of (PVA-PEG-PVP-MgO) and (PVA-PEG-PVP-CoO) Biomaterials, International Journal of Science and Research (IJSR) Volume 3 Issue 10, October 2014

[58] S. Choudhary, Characterization of amorphous silica nanofiller effect on the structural, morphological, optical, thermal, dielectric and electrical properties of PVA–PVP blend based polymer nanocomposites for their flexible nanodielectric applications. J. Mater. Sci.: Mate. Electron. (2018). https://doi.org/10.1007/s10854-018-9116-y

[59] M. I. Mohammed, S.S. Fouad, N. Metha. Dielectric relaxations and thermally activated a.c conduction in (PVDF) /(rGO) nanocomposites. Journal of Materials Science: Materials in Electronics V29, 18271–18281, 2018.

[60]S.N. Cassu, M.I. Felisberti, Poly(vinyl alcohol) and poly(vinylpyrrolidone) blends: Study of relaxations by dynamic mechanical analysis. Polymer 40 (1999) 4845–4851.

[61] R.J. Sengwa, S. Sankhla, S. Choudhary, Dielectric characterization of solution intercalation and melt intercalation poly(vinyl alcohol)–poly(vinyl pyrrolidone) blend–montmorillonite clay nanocomposite films. Indian J. Pure Appl. Phys. 48 (2010) 196–204.

[62] A.S. El-Houssiny, A.A.M. Ward, S.H. Mansour, S.L. Abd-El-Messieh, Biodegradable blends based on polyvinyl pyrrolidone for insulation purposes. J. Appl. Polym. Sci. 124 (2012) 3879–3891.

[63] N. Bouropoulos, G.C. Psarras, N. Moustakas, A. Chrissanthopoulos, S. Baskoutas, Optical and dielectric properties of ZnO-PVA nanocomposites. Phys. Stat. Sol. A 205 (2008) 2033–2037

[64] G.A. Kontos, A.L. Soulintzis, P.K. Karahaliou, G.C. Psarras, S.N. Georga, C.A.

Krontiras, M.N. Pisanias, Electrical relaxation dynamics in TiO_2–polymer matrix composites, Express Polym. Lett. 1 (2007) 781–789.

[65] Elhosiny Ali H, Abdel-Aziz MM, Nawar AM, et al. Structural, electrical, and nonlinear optical performance of PVAL embedded with Li+-ions for multifunctional devices. Polym Adv Technol. 2020;1–15. https://doi.org/10.1002/pat.5149

[66] Abkowitz M, Facci JS, Rehm J. Direct evaluation of contact injection efficiency into small molecule based transport layers: influence of extrinsic factors. J Appl Phys. 1998;83:2670-2676..

[67] N.M.A. Hadia, H.A.H. Mohamed, Characteristics and optical properties of MgO nanowires synthesized by solvothermal method, Mater. Sci. Semicond. Process. 29 (2015) 238–244, https://doi.org/10.1016/j.mssp.2014.03.049.

[68] K. Rajesh, V. Crasta, N.R. Kumar, G. Shetty, P.D. Rekha, Structural, optical, mechanical and dielectric properties of titanium dioxide doped PVA/PVP nanocomposite, J. Polym. Res. 26 (4) (2019) 99, https://doi.org/10.1007/s10965-019-1762-0.

List of Table*s*

Table.1: XRD Data for MgO / PVA- PVP nanocomposite films.

Samples	$2\theta^{\circ}$	d, (Å)	D, (nm)	δ, (A^{o})	Strain, (ε)	X_c, (%)
Pure PVA-PVP	19.77	4.489	3.73	7.168 x10^{-2}	9.28 x10^{-3}	24.68
0.06 wt% MgO	19.48	4.555	3.52	8.06 x10^{-2}	9.84 x10^{-3}	26.17
0.3 wt% MgO	19.73	4.498	4.03	6.14 x10^{-2}	8.59 x10^{-3}	22.85
0.6 wt% MgO	19.33	4.590	3.64	7.51 x10^{-2}	9.50 x10^{-3}	25.25
3.1 wt% MgO	20.27	4.379	4.05	6.07 x10^{-2}	8.54 x10^{-3}	22.74
6.25 wt% MgO	19.68	4.509	4.636	4.65 x10^{-2}	7.47 x10^{-3}	19.88

Table. 2: Mechanical characteristics of MgO / (PVA-PVP) nanocomposite films.

Samples	Young's modulus Y, (MPa)	Elongation at break, (ε %)	Tensile Strength (T.S) (MPa)
Pure PVA-PVP	51.1668	39.3	5.92
0.06 wt% MgO	54.339	43.7	6.7
0.3 wt% MgO	73.8964	52.69	7.7
0.6 wt% MgO	87.4587	59.58	7.95
3.1 wt% MgO	99.5781	75.26	9.44
6.25 wt% MgO	166.4063	81.4	10.65

Table 3: The indirect and direct band gap, the band tails energy of Urbach's, for (PVA–PVP)/ MgO polymeric nanocomposite films.

Samples	E_g (eV) Indirect	E_g (eV) Direct	$E_g(T)$	E_u, (eV)
Pure PVA-PVP	4.83	5.26	5.0344	1.015476
0.06 wt% MgO	4.8	5.2	4.9104	1.124872
0.3 wt% MgO	4.78	5.17	4.8484	1.20754
0.6 wt% MgO	4.72	5.15	4.7864	1.301643
3.1 wt% MgO	4.67	5.13	4.7492	1.482646
6.25 wt% MgO	4.02	4.96	4.5384	3.5891

Table 4: Values of dc electrical conductivity σ_{dc} and their corresponding fractional exponent s for the (PVA–PVP)–6.25 wt% MgO film at different temperatures T.

Temperature	σ_{dc} (S/m)	S
30 °C	5.1×10^{-9}	0.78
50 °C	3.38×10^{-8}	0.71
70 °C	9.58×10^{-8}	0.66
90 °C	1.86×10^{-7}	0.64
110 °C	2.66×10^{-7}	0.56
130 °C	3.66×10^{-7}	0.48

Table 5: The values of the nonlinear exponent parameters of the as-prepared polymer nanocomposites

Samples	ρ_1	ρ_2
Pure PVA-PVP	0.50519	0.98638
0.06 wt% MgO	0.85264	1.00135
0.3 wt% MgO	0.70611	1.11983
0.6 wt% MgO	1.01244	1.10453
3.1 wt% MgO	1.16666	1.63453
6.25 wt% MgO	1.25466	1.34255

Figures lists

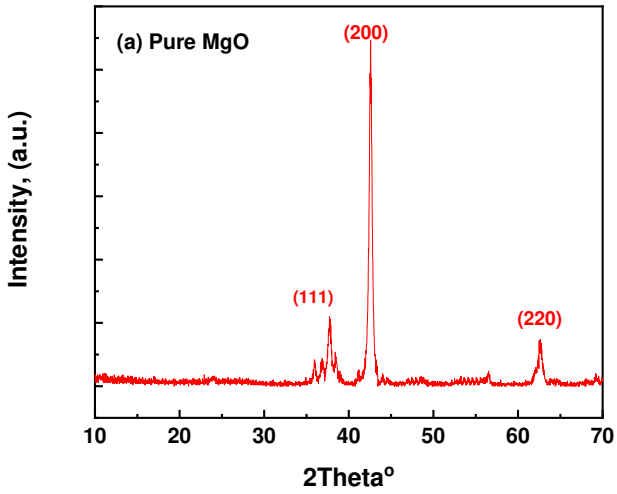

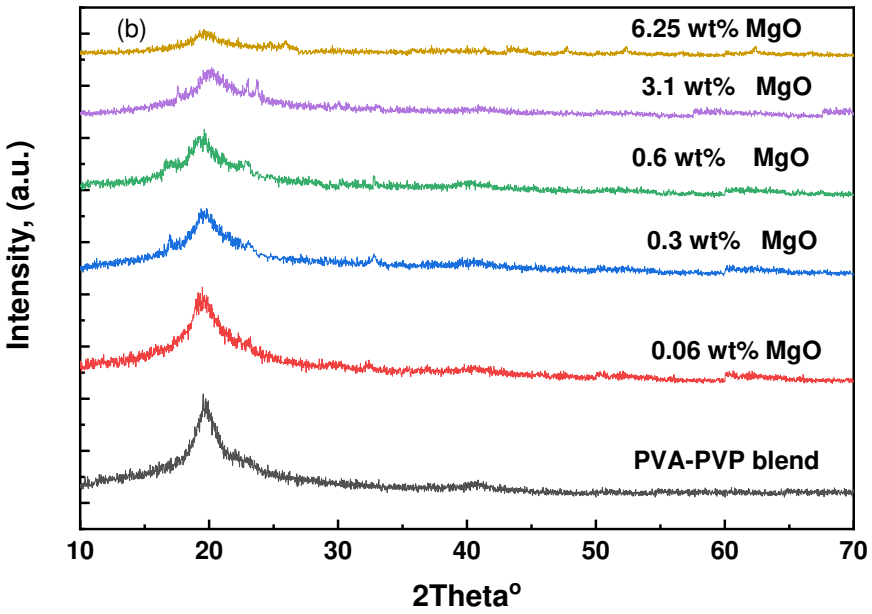

Fig. 1. (a) XRD patterns obtained for the MgO NPs and (b) for PVA/ PVP (blend), and the blends loaded with 0.06, 0.3, 0.6, 3.1 and 6.25 wt% MgO NPs.

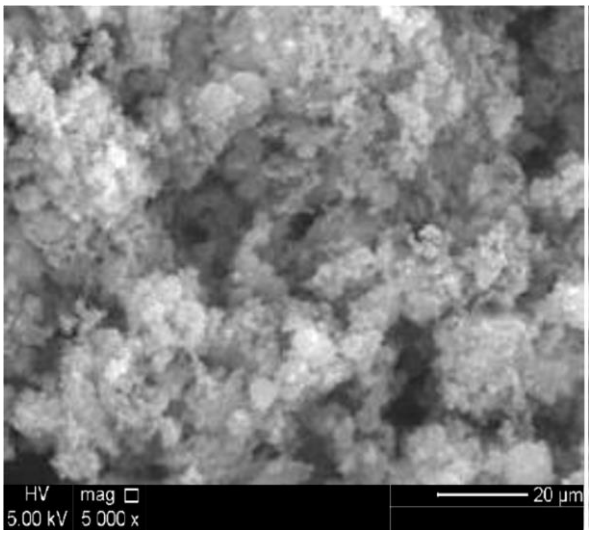

(a) Pure MgO NPs

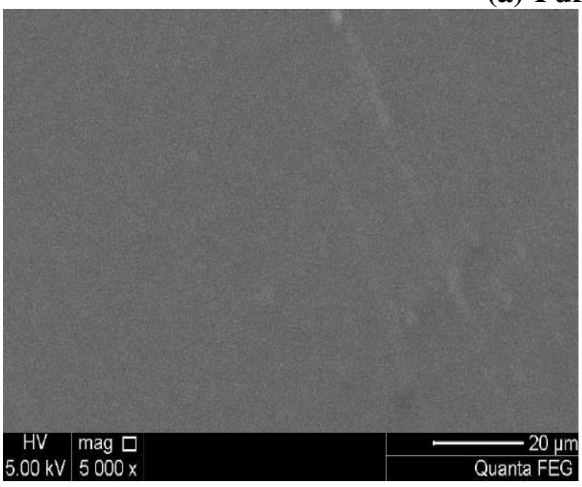

(b) Pure PVP/PVA (blend)

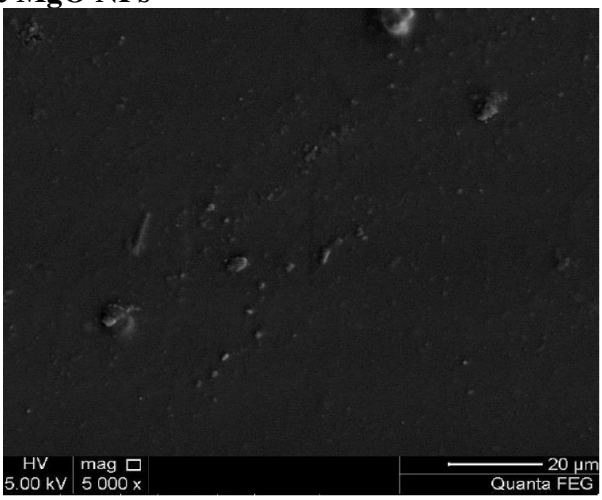

(c) 0.6 wt % MgO

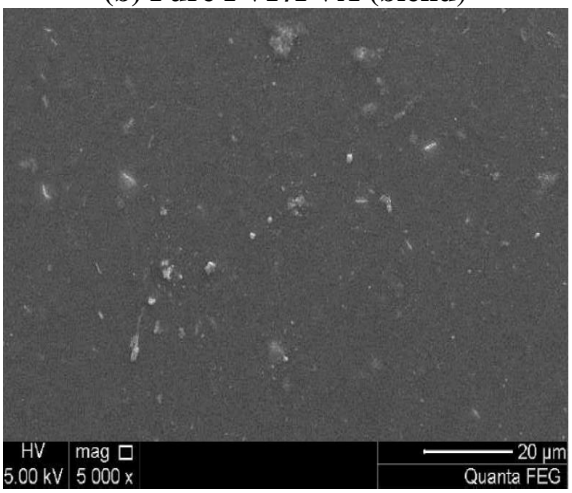

(d) 3.1 wt % MgO

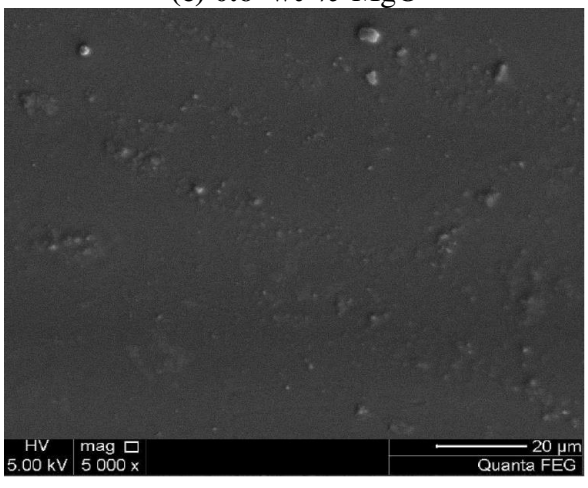

(e) 6.25 wt % MgO

Fig.2 : SEM micrograph of (a) nano-MgO. (b) pure PVA/PVP blend and PVA-PVP/ MgO nanocomposites with (c) 0.06 wt %, (d) 3.1 wt%, and (e) 6.25 wt% of MgO NPs.

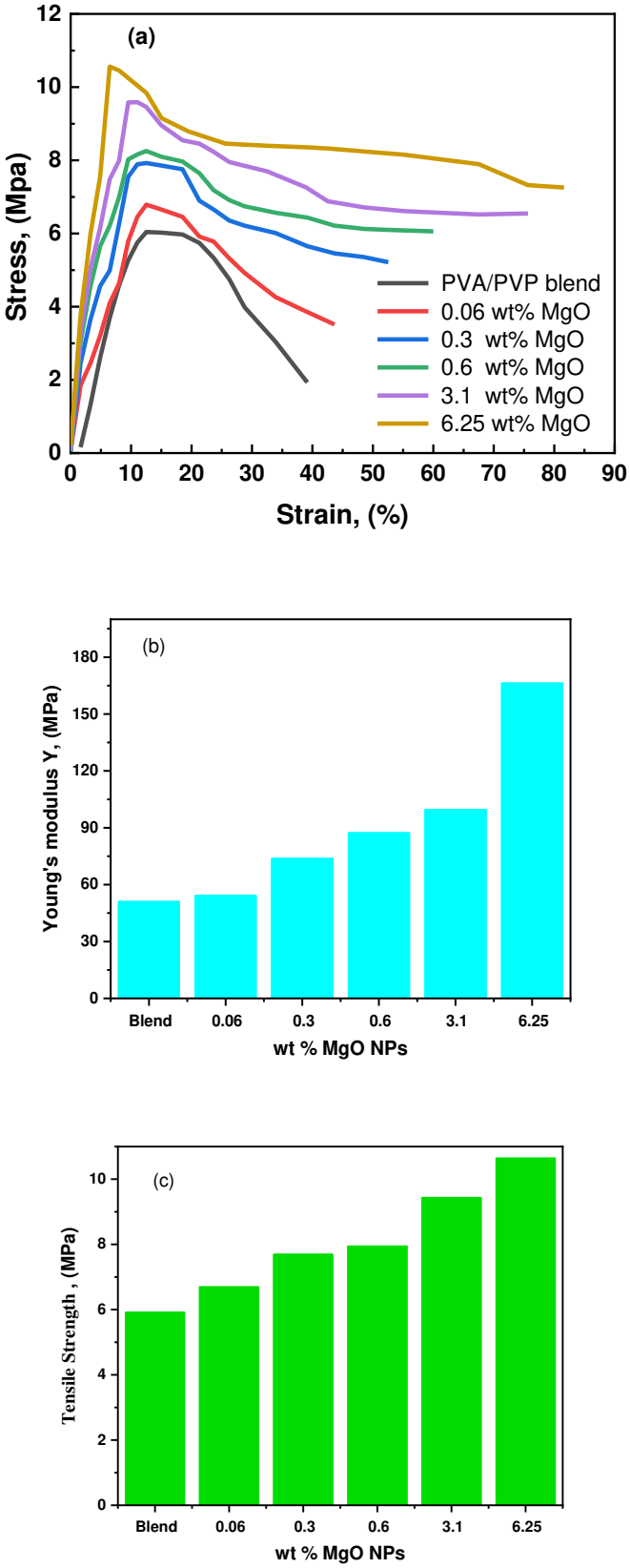

Fig.3: (a) The representative stress–strain curves, (b) Young's modulus , and (c) Tensile Strength of MgO/(PVA– PVP) nanocomposite films.

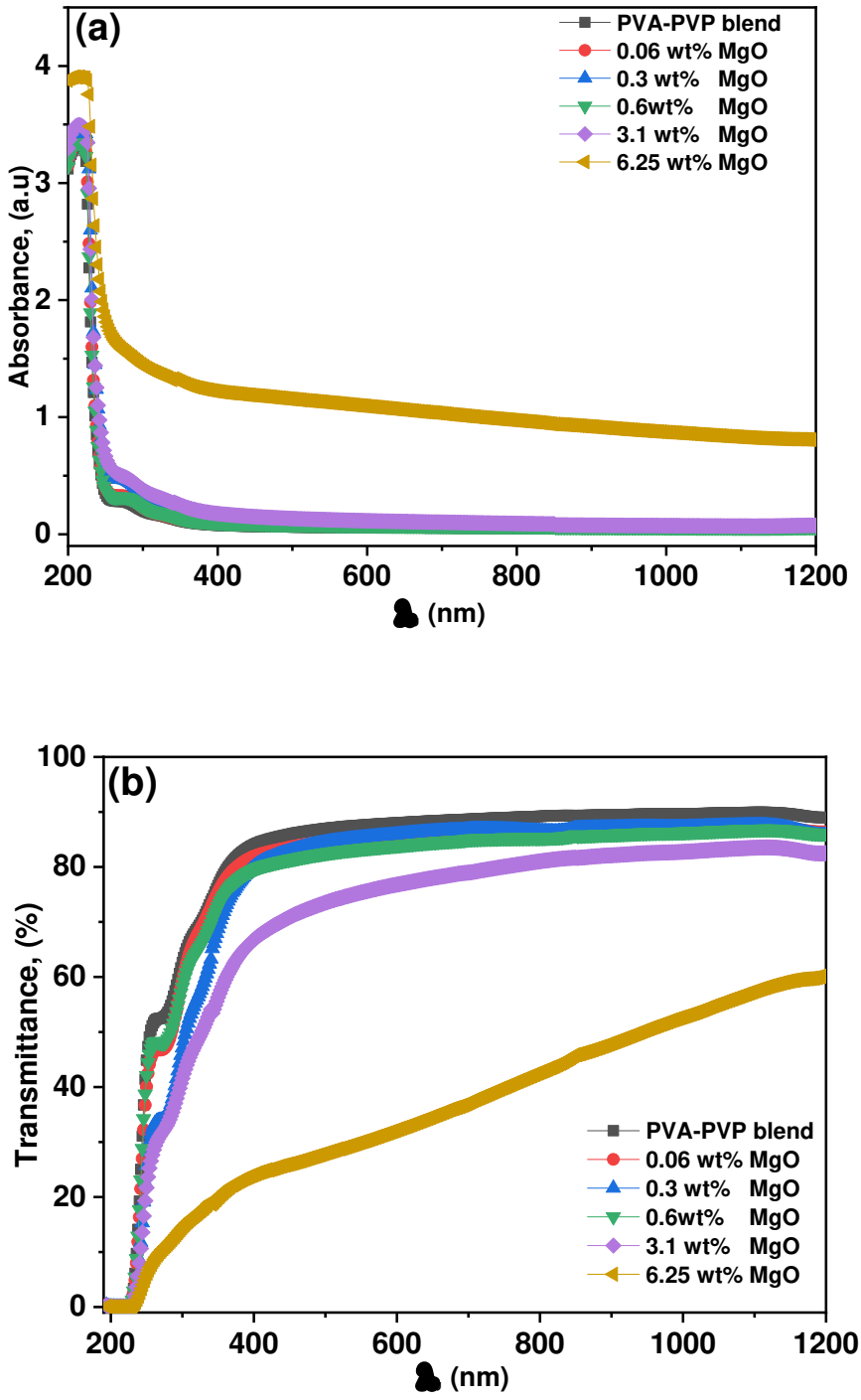

Fig.4: (a) Absorbance, and (b) Transmittance plots vs. λ for different nanocomposite samples.

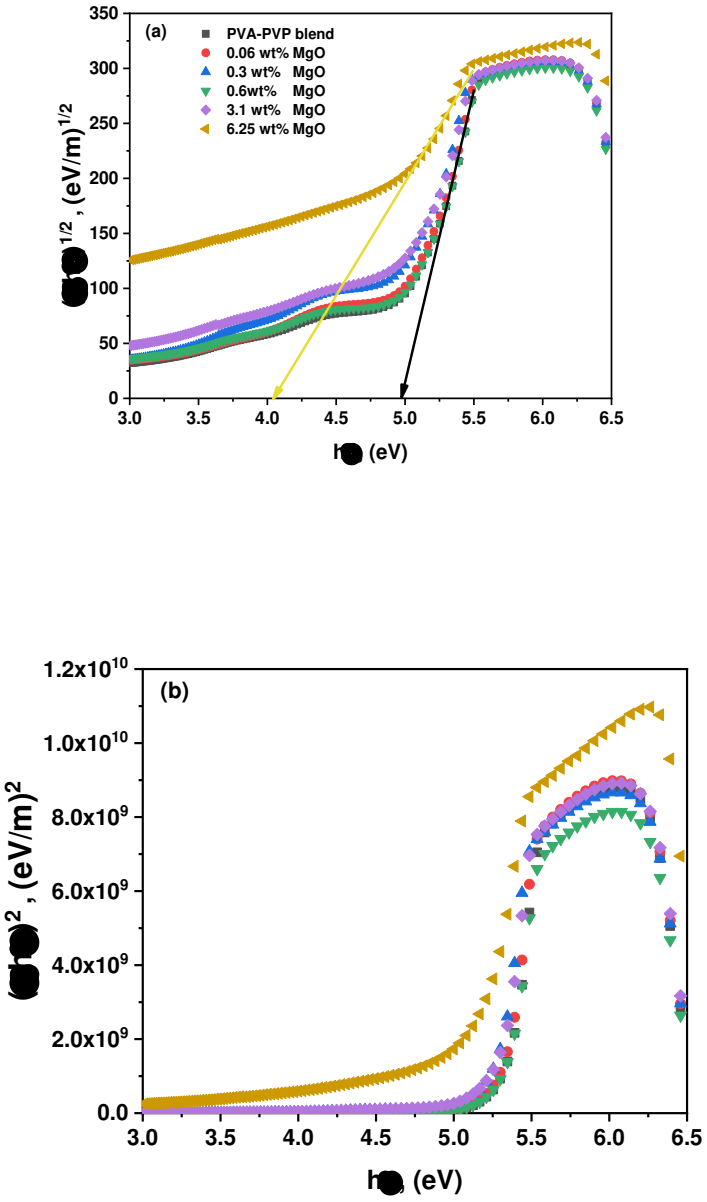

Fig. 5: Plots of (a) $(\alpha h\upsilon)^{1/2}$, and (b) $(\alpha h\upsilon)^2$ versus $(h\upsilon)$ for PVA-PVP/MgO nanocomposite films.

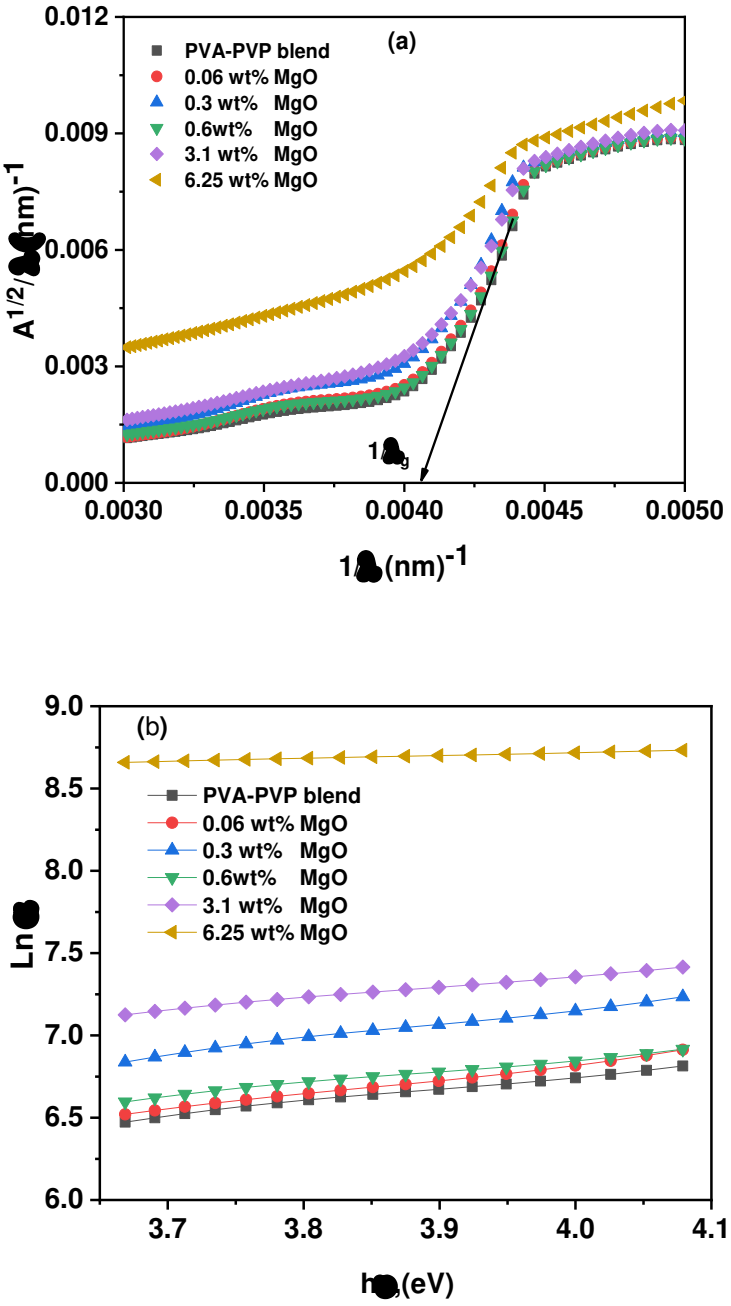

Fig.6: (a) $A^{1/2}/\lambda$ versus $1/\lambda$, and (b) the Urbach energy plot (lnα vs incident photon energy) for the prepared samples.

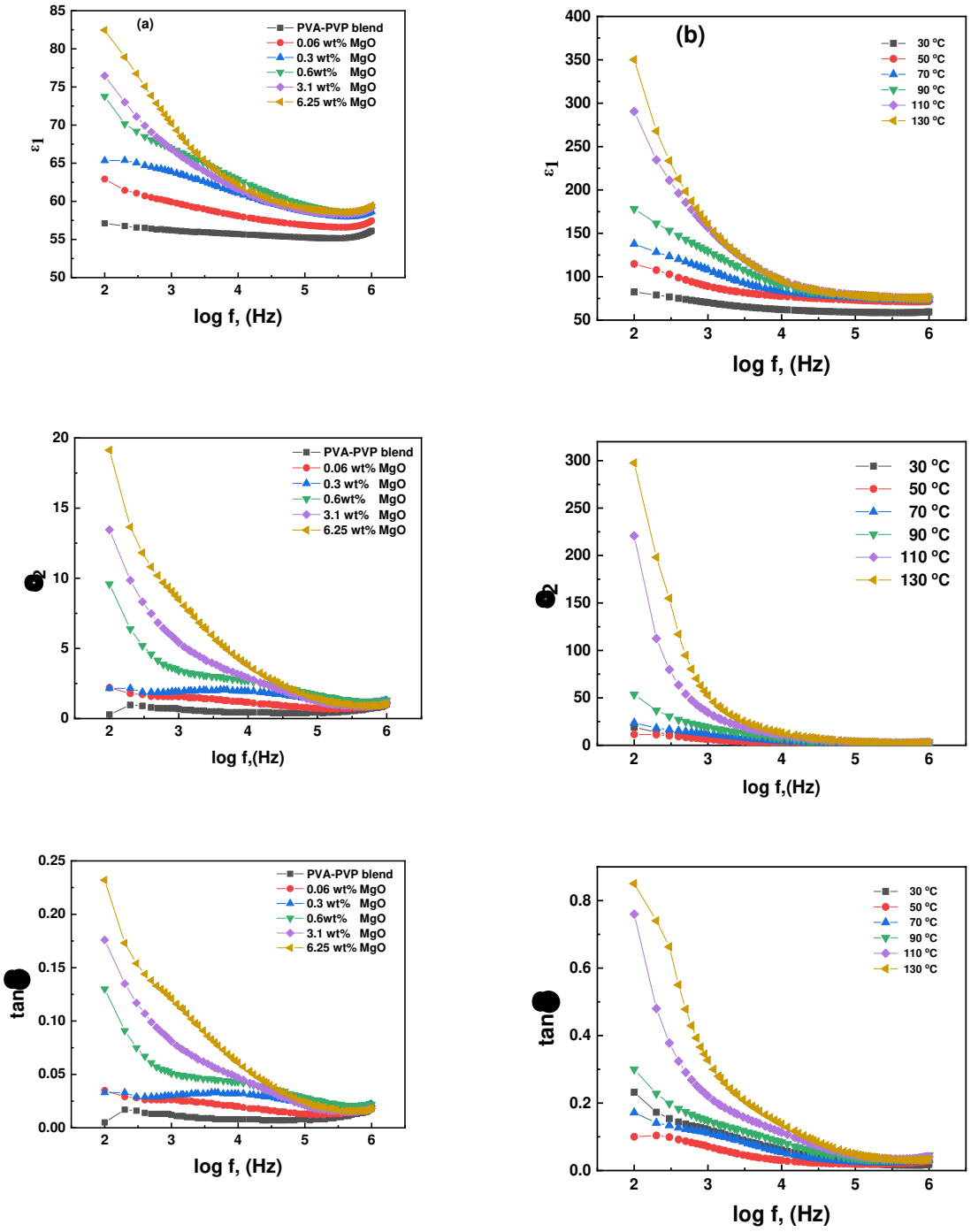

Fig. 7: Frequency dependent dielectric constant ε_1, dielectric loss ε_2 , and tanδ of (a) (PVA–PVP)/MgO nanocomposite films at 30°C, and (b) (PVA–PVP)– 6.25 wt% MgO – nanocomposite film at various temperatures.

.

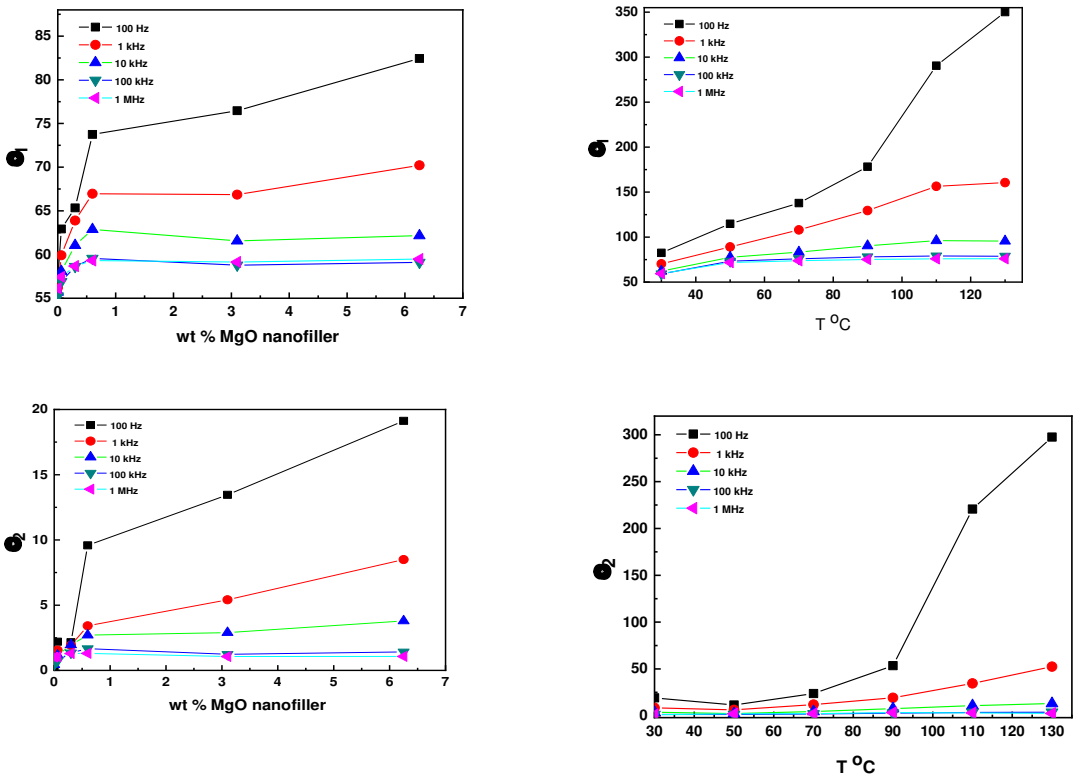

Fig.8: Plots of ε_1 and ε_2 values (a) C60 concentration dependent of (PVA– PVP)– MgO nanocomposite films at 30°C and (b) (PVA–PVP)–6.25 wt% MgO nanocomposite film at various temperatures at several frequencies.

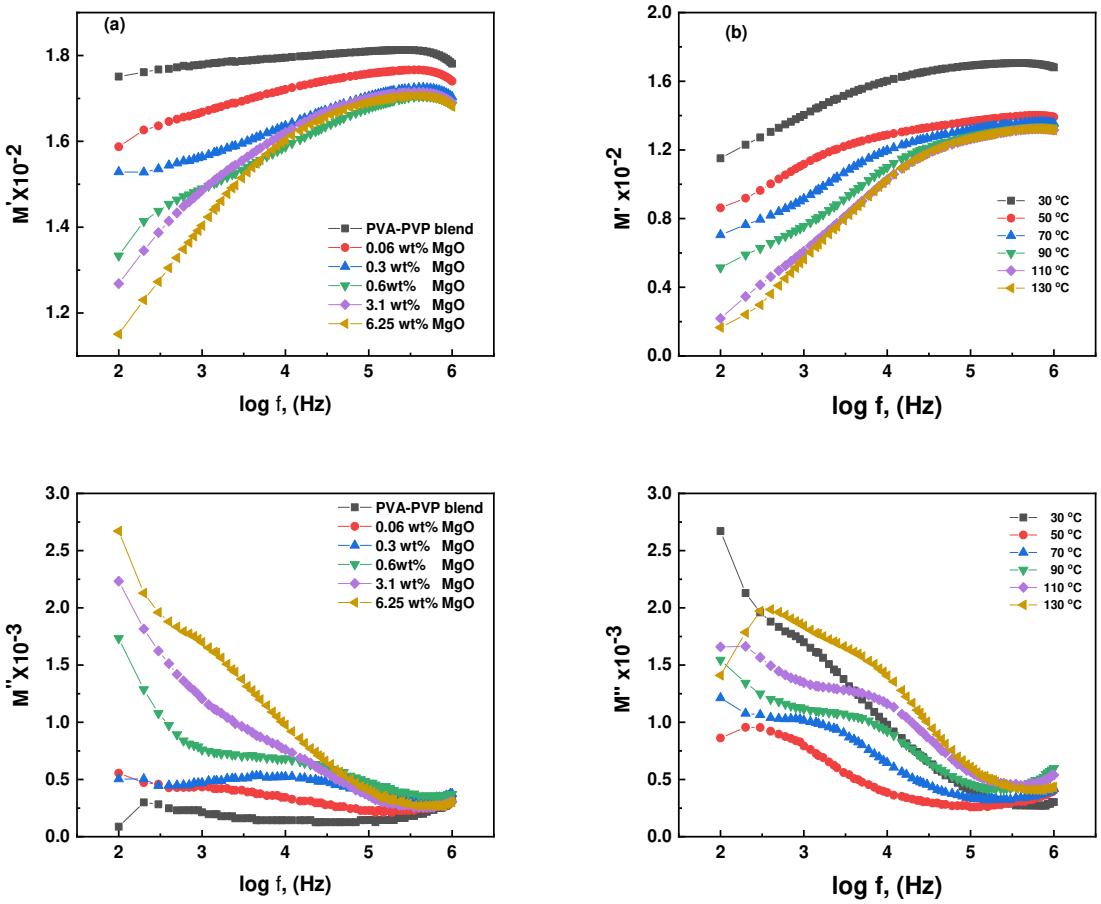

Fig.9: Frequency dependent real part M' and loss part M'' of complex electric modulus of (a) (PVA–PVP)/MgO nanocomposite films at 30°C, and (b) (PVA–PVP)– 6.25 wt% MgO –nanocomposite film at various temperatures.

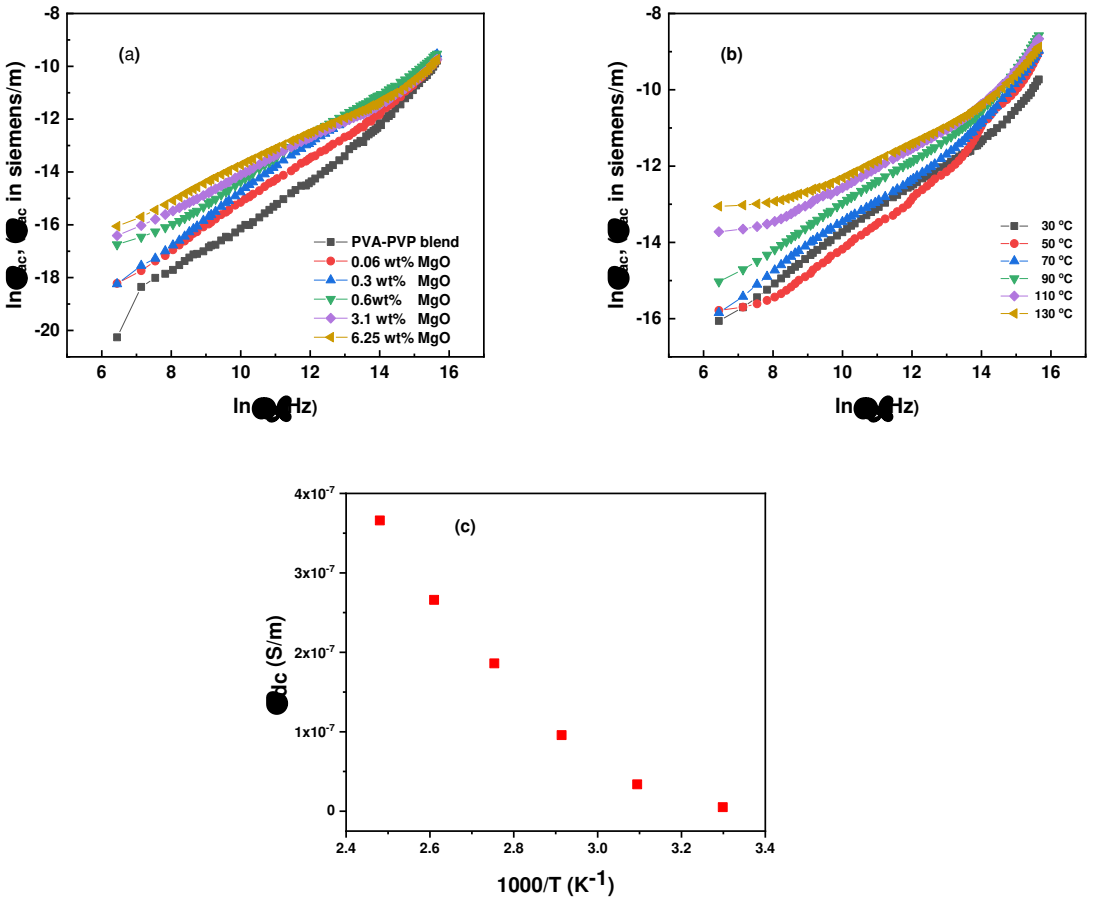

Fig. 10: Frequency dependent ac electrical conductivity (a) (PVA–PVP)/MgO nanocomposite films at 30°C, (b) (PVA–PVP)– 6.25 wt% MgO –nanocomposite film at various temperatures, and (c) Arrhenius plots of the dc conductivity σ_{dc} of (PVA–PVP)–6.25 wt% MgO polymeric nanocomposite film**.**

.

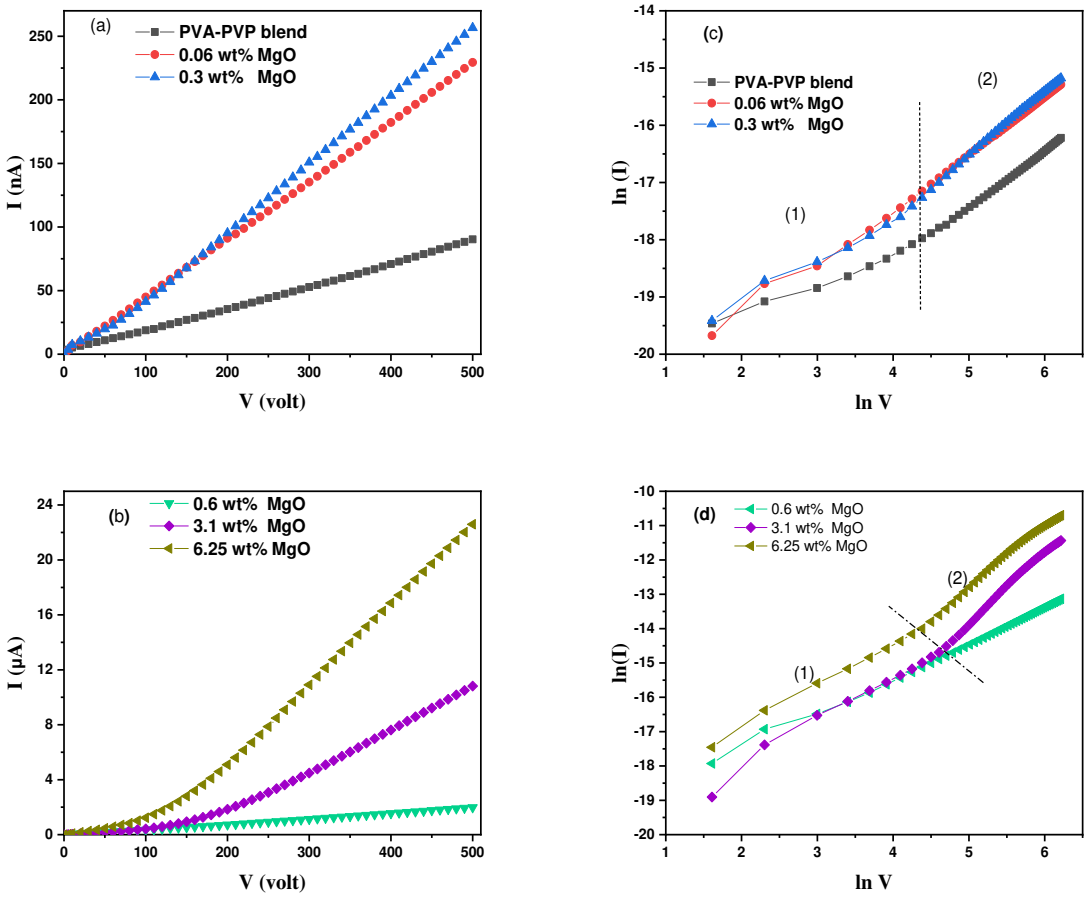

Fig. 11: Variation of current (I) -voltage (V) plots and the corresponding ln(I)-ln(V) plots of MgO / (PVA- PVP) polymeric nanocomposite films.